Manuscript prepared for Atmos. Meas. Tech.
with version 4.2 of the LaTeX class copernicus.cls.
Date: 26 May 2017

Joint retrieval of surface reflectance and aerosol properties with continuous variation of the state variables in the solution space: Part 1: theoretical concept

Yves Govaerts[1] and Marta Luffarelli[1]

[1]Rayference, Brussels, Belgium

Correspondence to: Yves Govaerts (yves.govaerts@rayference.eu)

Abstract. This paper presents a new algorithm for the joint retrieval of surface reflectance and aerosol properties with continuous variations of the state variables in the solution space. This algorithm, named CISAR (Combined Inversion of Surface and AeRosol), relies on a simple atmospheric vertical structure composed of two layers and an underlying surface. Surface anisotropic reflectance effects are taken into account and radiatively coupled with atmospheric scattering. For this purpose, a fast radiative transfer model has been explicitly developed, which includes acceleration techniques to solve the radiative transfer equation and to calculate the Jacobians. The inversion is performed within an optimal estimation framework including prior information on the state variable magnitude and regularization constraints on their spectral and temporal variability. In each processed wavelength, the algorithm retrieves the parameters of the surface reflectance model, the aerosol total column optical thickness and single scattering properties. The CISAR algorithm functioning is illustrated with a series of simple experiments.

1 Introduction

Radiative coupling between atmospheric scattering and surface reflectance processes prevents the use of linear relationships for the retrieval of aerosol properties over land surfaces. The discrimination between the contribution of the signal reflected by the surface and that scattered by aerosols represents one of the major issues when retrieving aerosol properties using spaceborne imager observations over land surfaces. Conceptually, this problem is equivalent to solving a radiative system composed of at least two layers, where the upper layers include aerosols and the bottom ones represent the soil/vegetation strata. The problem is further complicated by the intrinsic anisotropic radia-

tive behaviour of natural surfaces due to the mutual shadowing of the scattering elements, which is also affected by the amount of sky radiation (Govaerts et al., 2010, 2016). In most cases, an increase in aerosol concentration is responsible for an increase in the fraction of diffuse sky radiation which, in turn, smooths the effects of surface reflectance anisotropy. Though multi-spectral information

25   is critical for the retrieval of aerosol properties, the spectral dimension alone does not allow full characterisation of the underlying surface reflectance which often offers a significant contribution to the total signal observed at the satellite level. In this regard, the additional information contained in multi-spectral and multi-angular observations through the joint retrieval of surface reflectance and aerosol properties has proven to be an efficient way to characterize aerosol properties over land

30   surfaces.

Pinty et al. (2000a) pioneered the development of a retrieval method dedicated to the joint retrieval of surface reflectance and aerosol properties based on the inversion of a physically-based radiative model. This method has been subsequently improved to allow the processing of any geostationary satellites accounting for their actual radiometric performance (Govaerts and Lattanzio, 2007).

35   This new versatile version of Pinty's algorithm has permitted the generation of a global surface albedo product from archived data acquired by operational geostationary satellites around the globe (Govaerts et al., 2008). These data included observations acquired by an old generation of radiometers with only one broad solar channel on-board the European Meteosat First Generation satellite, the US Geosynchronous Operational Environmental Satellite (GOES) and the Japanese Geostation-

40   ary Meteorological Satellite (GMS). It is now routinely applied in the framework of the Sustained and COordinated Processing of Environmental satellite data for Climate Monitoring (SCOPE-CM) initiative for the generation of essential climate variables (Lattanzio et al., 2013). An improved version of this algorithm has been proposed by Govaerts et al. (2010) to take advantage of the multi-spectral capabilities of Meteosat Second Generation Spinning Enhanced Visible and Infrared

45   Imager (MSG/SEVIRI) operated by EUMETSAT, and includes an Optimal Estimation (OE) inversion scheme using a minimization approach based on the Marquardt-Levenberg method (Marquardt, 1963).

The strengths and weaknesses of the algorithm proposed by Govaerts et al. (2010) are discussed in Section (2). In their proposed approach, the solutions of the Radiative Transfer Equation (RTE) are

50   pre-calculated and stored in Look-Up Tables (LUTs) for a limited number of state variable values. Aerosol properties are limited to six different classes dominated either by fine or coarse particles. Two major drawbacks result from the use of pre-defined aerosol classes stored in pre-computed LUTs. Firstly, only a limited region of the solution space is sampled as a result of the reduced range of variability for state variables. For instance, in order to reduce the size of the LUTS, Pinty et al.

55   (2000b) limit the maximum aerosol optical thickness to 1. Secondly, the solution space is not continuously sampled due to the use of pre-defined aerosol classes. Such an approach prevents an accurate retrieval of the solution at the expense of a very large number of classes. Dubovik et al. (2011) and

Diner et al. (2012), among others, demonstrated the advantages of a retrieval approach based on continuous variations of the aerosol properties as opposed to a LUT-based approach relying on a set
60 of pre-defined aerosol classes. Even considering a large number of aerosol classes, LUT-based approaches under-perform methods with multi-variate continuity in the solution space (Kokhanovsky et al., 2010).

A new joint surface reflectance / aerosol properties retrieval approach is presented here that overcomes the limitations resulting from pre-computed RTE solutions stored in LUTs. This new method
65 takes advantage of the lessons learned from past attempts to retrieve simultaneously surface reflectance and aerosol properties. The advantages of a continuous variation of the aerosol properties in the solution space against a LUT-based approach is discussed in Section (3). The proposed method expresses the scattering albedo and phase function values as a linear mixture of basic aerosol classes. The forward radiative transfer model that includes the Jacobians computation is described in Section
70 (4). With the exception of gaseous transmittance, this model no longer relies on LUTs, and the RTE is explicitly solved. The inversion method is described in Section (5). Finally, the possibility to express aerosol single scattering properties as a linear combination is illustrated with simulated data representing various scenarios including small and large particles (6).

2 Lessons learned from previous approaches

75 Pinty et al. (2000a) proposed an algorithm for the joint retrieval of surface reflectance and aerosol properties to demonstrate the possibility of generating Essential Climate Variables (ECV) from data acquired by operational weather geostationary satellites. Due to limited operational computational resources available at that time in the EUMETSAT ground segment, where the data were processed, the development of this algorithm was subject to strong constraints. The RTE solutions were pre-
80 computed and stored in LUTs with a very coarse resolution, limiting the maximum Aerosol Optical Thickness (AOT) to 1, which represented a severe limitation over the Sahara region where AOT values can easily exceed such limit. Furthermore, the radiative coupling between aerosol scattering and gaseous absorption was not taken into account. This algorithm, referred to as Geostationary Surface Albedo (GSA) has been subsequently modified by Govaerts and Lattanzio (2007) to include
85 an estimation of the retrieval uncertainty. This updated version has permitted the generation of a global aerosol product derived from observations acquired by operational weather geostationary satellites (Govaerts et al., 2008). Since then, it is routinely applied in the framework of the SCOPE-CM initiative to generate a Climate Data Record (CDR) of surface albedo (Lattanzio et al., 2013).

The GSA algorithm has been further improved for the processing of SEVIRI data on-board MSG
90 for the retrieval of the total column AOT from observations acquired in the VIS0.6, VIS0.8 and NIR1.6 spectral bands (Govaerts et al., 2010; Wagner et al., 2010). The method developed by these authors relies on an OE approach where surface reflectance and daily aerosol load are simultaneously

retrieved. The inversion is performed independently for each aerosol class and the one with the ==best fit== is selected. A physically-based radiative transfer model accounting for non-Lambertian surface

95 reflectance and its radiative coupling with atmospheric scattering is inverted against daily accumulated SEVIRI observations. However, this Land Daily Aerosol (LDA) algorithm suffers from two major limitations: (*i*) the use of pre-defined aerosol classes and, (*ii*) the algorithm delivers only one mean aerosol value per day when applied on MSG/SEVIRI data. This latter issue has been addressed by Luffarelli et al. (2016) who retrieve an aerosol optical thickness value for each SEVIRI obser-

100 vation. The former issue prevents a continuous variations of the state variables characterizing the aerosol single scattering properties ==as required by an OE approach (Rodgers, 2000).== A consistent implementation of such approach is not straightforward since aerosol classes are defined as prior knowledge of the observed medium ==but no uncertainties are assigned to this information.== Consequently, the estimated ~~retrieval~~ retrieval uncertainty is inconsistent as it does not account for the use

105 ==of prior information and associated uncertainties.==
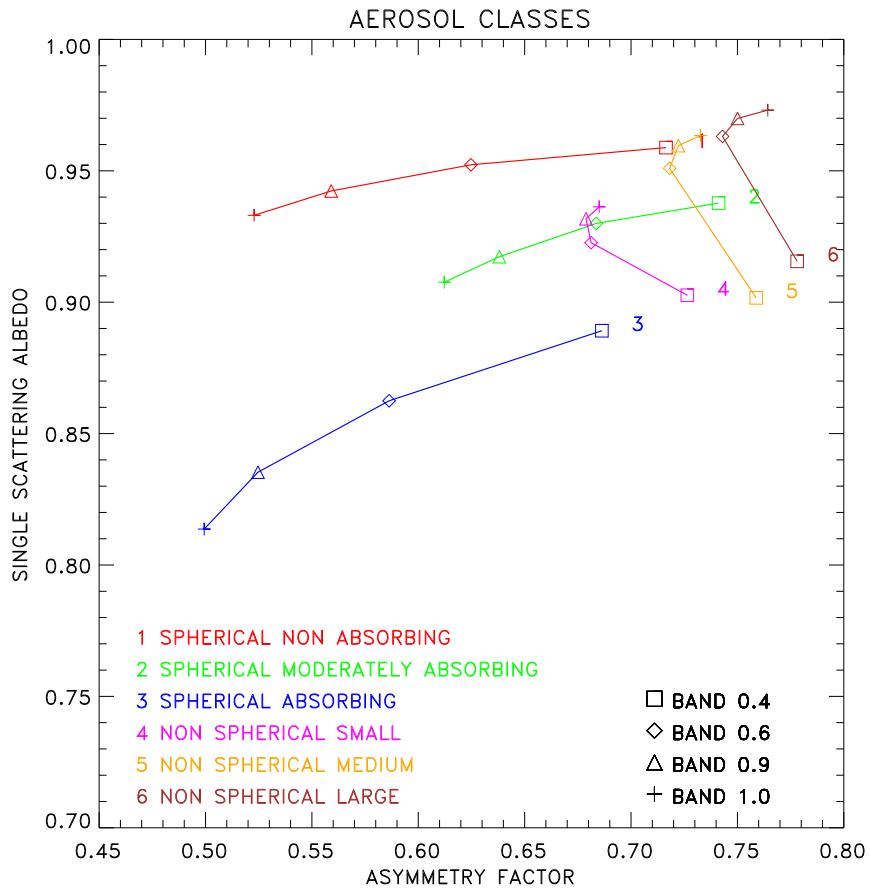
Fig. 1. Aerosol dual mode classes after Govaerts et al. (2010) in the $[g, \omega_0]$ space derived from the aggregation of aerosol single scattering properties retrieved from AERONET observations (Dubovik et al., 2006). Classes 1 to 3 are dominated by the fine mode and 4 to 6 by the coarse one.

Diner et al. (2012) demonstrated the advantages of a retrieval method based on continuous variations of aerosol single scattering properties in the solution space as opposed to a LUT-based approach derived for a limited number of pre-defined aerosol classes. Dubovik et al. (2011) proposed an original method for the retrieval of aerosol micro-physical properties which also does not necessitate the use of predefined aerosol classes. This method retrieved more than 100 state variables requiring therefore a considerable number of observations, such as those provided by multi-angular and -polarisation radiometers like Polarisation et Anisotropie des Réflectances Au SOmmet de l'Atmosphère (PARASOL) (Serene and Corcoral, 2006) or the future Multi-viewing Multi-channel Multi-polarization Imaging (3MI) instrument on-board EUMETSAT's Polar System Second Generation (Manolis et al., 2013). Instruments delivering such a large number of observations are rather scarce as most of the current or planned passive optical sensors do not offer instantaneous multi-angular observation capabilities nor information on polarization. The primary objective of this paper is to address the limitations resulting from conventional approaches based on LUTs and/or a limited number of pre-defined aerosol classes, proposing a method that can be applied to observations acquired by single or multi-view instruments.

3 Continuous variation of aerosol properties in the solution space

Aerosol single scattering properties include the single scattering albedo ω_0 and the phase function Φ in RTE. Govaerts et al. (2010) explained the benefits of representing pre-defined aerosol classes in a two-dimensional solution space composed of these aerosol single scattering properties. For the sake of clarity, they limited the phase function in that 2D space to the first term of the Legendre coefficients, *i.e.*, the asymmetry parameter g. However, one should keep in mind that the reasoning applied in this Section should be applied on the entire phase function Φ. These aerosol single scattering properties are themselves determined by aerosol micro-physical properties such as the particle size distribution, shape and their complex index of refraction. Within a retrieval approach based on aerosol classes, the objective is to provide the best possible sampling of the $[g, \omega_0]$ space such as in Govaerts et al. (2010). The inversion process proposed by these authors relies on a set of six classes which have been defined from AErosol RObotic NETwork (AERONET) data aggregation (Dubovik et al., 2006). These classes are supposed to provide the most likely sampling of the solution space but, since the scattering properties are not continuously varied, the inversion is typically repeated for each aerosol class and the one with the best fit is selected (Wagner et al., 2010).

A visual inspection of Fig. (1) after Govaerts et al. (2010) reveals that aerosol classes occupy different regions in the $[g, \omega_0]$ space according to the dominant particle size distribution, *i.e.*, fine or coarse. Within that space, an aerosol class is defined by the spectral behaviour of $\{g(\lambda), \omega_0(\lambda)\}$ pairs. The proposed fine mode classes vary mostly as a function ω_0 which is largely determined by the imaginary part of the refractive index n_i. Conversely, aerosol classes dominated by coarse
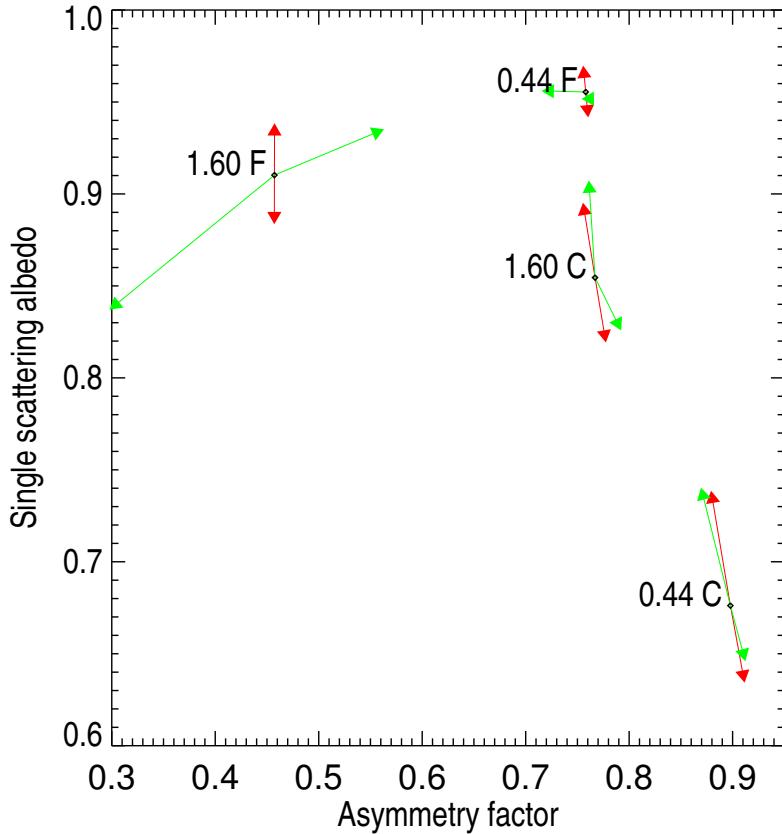
Fig. 2. Example of sensitivity of aerosol single scattering properties to particle median radius (green arrows) and imaginary part of the refractive index (red arrows) at 0.44μm and 1.60μm for fine mode F ($r_{mf} = 0.1\mu m$) and coarse mode C ($r_{mc} = 2.0\mu m$).

particles show little dependency on g and are therefore organised parallel to the ~~single scattering albedo~~ axis. The main parameter discriminating the~~se latter~~ classes is the median radius r_m, which essentially determines the asymmetry parameter value at a given wavelength λ.

To illustrate the dependence of g and ω_0 on the median radius r_m and imaginary part of the refractive index n_i, fine and coarse mono-mode aerosol classes ~~have been~~ generated with $r_m = 0.15\mu$m and 2.0μm respectively. The other micro-physical values ~~have been~~ fixed to $\sigma_r = 0.5\mu m$ $n_r = 1.42$ and $n_i = 0.008$ where σ_r is the radius standard deviation and n_r the real part of the refractive index. These values have been selected ~~on purpose~~ to ease the explanation of the aerosol classes organisation ~~on~~ Fig. (1). Black dots ~~on~~ Fig. (2) show the corresponding location ~~of the pair~~ of $\{g(\lambda), \omega_0(\lambda)\}$ ~~values~~ at 0.44μm and 1.60μm. Red arrows illustrate the sensitivity to a n_i change of ±0.0025 and the green ones to a r_m change of $\pm25\%$. For the fine mono-mode (F), changes in n_i essentially translate in displacement parallel to the ω_0 axis at short wavelengths while changes in

r_m result in changes parallel to the g axis. There is also a clear relationship between the particle size and g for that mode. A change in the particle size results in a change in g while ω_0 remains almost

155   unchanged. The situation is quite different for the coarse mono-mode where changes in both n_i and r_m induce displacement parallel to the ω_0 axis with limited impact on g values. It should also be noted that the direction and magnitude of the changes depend on the wavelengths.
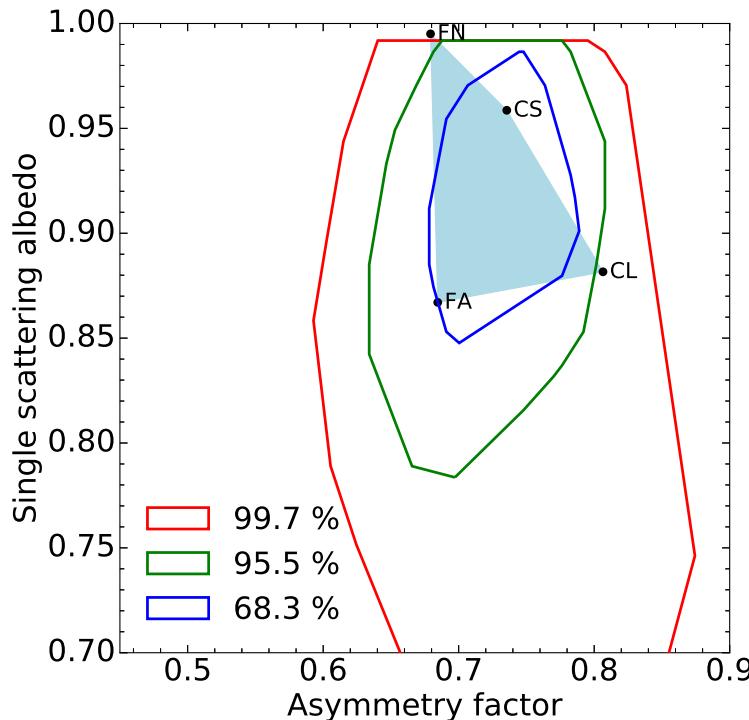
Fig. 3. Example of region (light blue area) in the $[g,\omega_0]$ solution space at $0.44\mu m$ defined by four aerosol vertices: single fine mode non-absorbing (FN), single fine mode absorbing (FA), coarse mode with small radius (CS) and coarse mode with large radius (CL). The isolines show the probability that the aerosol single scattering properties derived from Dubovik et al. (2006) fall within the delineated spaces.

The actual extent of possible solutions in the $[g,\omega_0]$ space for a given spectral band can be outlined by a series of vertices characterizing aerosol single scattering properties. Following Fig. (2), these

160   vertices are defined by an absorbing and a non-absorbing fine mono-mode classes with a small radius, labelled respectively FA and FN and by two coarse mono-modes with different radii, *i.e.*, large and small, labelled respectively CL and CS. Such vertices define a polygon within the $[g,\omega_0]$ solution space (Fig. 3). The number of vertices can be adjusted according to the amount of spectral observations and expected type of aerosols. In Section (4), we will see how any pair of single

165   scattering albedo and phase function values in that space can be expressed as a linear combination of the vertex properties.

The choice of the position of these vertices is critical as they should encompass most likely aerosol

single scattering properties that could be observed at a given time and location. ~~Different approaches could be used to define the position of these vertices.~~ These positions could be derived from the analysis of typical aerosol single scattering properties available in databases such as Optical Properties of Aerosols and Clouds (OPAC) (Hess et al., 1998). Alternatively, it is also possible to follow a similar approach as the one proposed in Govaerts et al. (2010) who analysed the single scattering albedo and phase function values derived from AERONET observations acquired in a specific region of interest for a given period (Dubovik et al., 2006). ~~Fig. (3) shows an example of such type of analysis performed in the blue spectral region.~~ The red isoline on that Fig. delineates the area of the $[g, \omega_0]$ space where 99.7% of the aerosol single scattering properties derived by Dubovik et al. (2006) from AERONET observations are located. The green and blue lines show respectively the 95% and 68% probability regions. These values have been derived using all available Level 2 AERONET observations since 1993. Finally, the model proposed by Schuster et al. (2005) can be used to determine the spectral variations of the single scattering properties outside the spectral bands measured by AERONET. The present study relies on simulated data and the aerosol vertices have been positioned to sample the solution space in a realistic way. In case of the processing of actual satellite data over a specific region or period, it is advised to calculate the isolines corresponding to that region of interest from AERONET observations and to adjust the position of the aerosol vertices accordingly.

4 Forward Radiative Transfer Model

4.1 Overview

The forward model, named FASTRE, simulates the TOA Bidirectional Reflectance Factor (BRF) $y_m(\mathbf{x}, \mathbf{b}; \mathbf{m})$ as a function of independent parameters $\mathbf{m}$ defining the observation conditions and a series of state variables $\mathbf{x}$ describing the state of the atmosphere and underlying surface. Model parameters $\mathbf{b}$ represent variables such as total column water vapour that ~~influence the value of $y_m(\mathbf{x}, \mathbf{b}; \mathbf{m})$ but~~ cannot be retrieved ~~from the processed space-based observations~~ due to the lack of independent information. The independent parameters $\mathbf{m}$ include the illumination and viewing geometries (Ω_0, Ω_v) and the ~~spectral bands~~ $\tilde{\lambda}$. The RTE is solved with the Matrix Operator Method (Fischer and Grassl, 1984) optimised by Liu and Ruprecht (1996) for a limited number of quadrature points.

The model simulates observations acquired within spectral bands $\tilde{\lambda}$ characterized by their spectral response. Gaseous transmittances in these bands are precomputed and stored in LUTs. ~~All other operations are calculated on the fly.~~ The model computes the contributions from single and multiple scattering separately, the latter being solved in Fourier space. In order to reduce the computation time, the forward model relies on the same atmospheric vertical structure as in Govaerts et al. (2010), *i.e.*, a three-level system containing two layers that are radiatively coupled (Fig. 4). The lowest level,
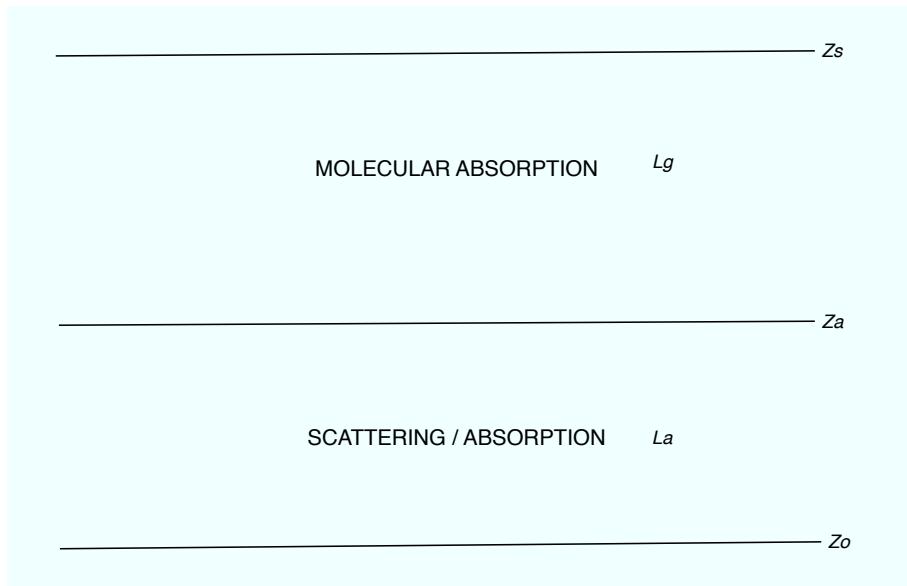
Fig. 4. Vertical structure of the FASTRE model. The surface is at level Z_0 and radiatively coupled with the lower layer L_a running from level Z_0 to Z_a. This layer includes scattering and absorption processes. The upper layer L_g runs from level Z_a to Z_s and only accounts for absorption processes.

Z_0, represents the surface. The lower layer L_a, ranging from levels Z_0 to Z_a, contains the aerosol particles. Molecular scattering and absorption are also taking place in that layer which is radiatively coupled with the surface for both the single and the multiple scattering. The upper layer L_g, ranging from Z_a to Z_s, is only subject to molecular absorption. It is assumed that no scattering processes are taking place in that layer.

The surface reflectance $r_s(\mathbf{x_s}, \mathbf{b}; \mathbf{m})$ over land is represented by the so-called RPV (Rahman-Pinty-Verstraete) model which has four parameters $\mathbf{x_s} = \{\rho_0, k, \Theta, h\}$ that are all wavelength dependent (Rahman et al., 1993). Each of these parameters control surface BRF differently. The ρ_0 parameter, included in the [0,1] interval, controls the mean amplitude of the BRF and strongly varies with wavelengths. The k parameter is the modified Minnaert's contribution that determines the bowl or bell shape of the BRF and it typically varies between 0 and 2. The asymmetry parameter of the Henyey-Greenstein phase function, Θ, varies between -1 and 1. The h parameter controls the amplitude of the hot-spot due to the "porosity" of the medium. This parameter takes only positive values and generally varies between 0 and 1. For the simulations over the ocean, the Cox-Munk model (Cox and Munk, 1954) is implemented (Vermote et al., 1997).

Aerosol single scattering properties in the layer L_a are represented by an external mixture of a series of predefined aerosol vertices as explained in Section (4.2). The L_g layer contains only absorbing gas not included in the scattering layer, such as high-altitude ozone, the part of the total column water vapour not included in layer L_a and few well-mixed gases.

The FASTRE model expresses the TOA BRF in a given spectral band $\tilde{\lambda}$ as a sum of the single $I_s^\uparrow$ and multiple $I_m^\uparrow$ scattering contributions as in

$$y_m(\mathbf{x},\mathbf{b};\mathbf{m}) = T_{L_g}(\mathbf{b};\mathbf{m}) \frac{I_s^\uparrow(\mathbf{x},\mathbf{b};\mathbf{m}) + I_m^\uparrow(\mathbf{x},\mathbf{b};\mathbf{m})}{E_0^\downarrow(\mathbf{m})\mu_0} \tag{1}$$

where

. $I_s^\uparrow(\mathbf{x},\mathbf{b};\mathbf{m})$ is the upward radiance field at level Z_a due to the single scattering;

. $I_m^\uparrow(\mathbf{x},\mathbf{b};\mathbf{m})$ is the upward radiance field at level Z_a due to the multiple scattering;

225 . $T_{L_g}(\mathbf{b};\mathbf{m})$ denotes the total transmission factor in the L_g layer;

. $E_0^\downarrow(\mathbf{m})$ denotes the solar irradiance at level Z_s corrected for the Sun-Earth distance variations.

The single scattering contribution writes

$$I_s^\uparrow(\mathbf{x},\mathbf{b};\mathbf{m}) = \frac{E_0^\downarrow(\mathbf{m})\,\mu_0}{\pi} \exp\left(\frac{-\tau_{L_a}}{\mu_0}\right) r_s(\mathbf{x_s},\mathbf{b};\mathbf{m}) \exp\left(\frac{-\tau_{L_a}}{\mu_v}\right) \tag{2}$$

where τ_{L_a} is the total optical thickness of layer L_a. μ_0 and μ_v are the cosine of the illumination and viewing zenith angles respectively.

The multiple scattering contribution $I_m^\uparrow(\mathbf{x},\mathbf{b};\mathbf{m})$ is solved in the Fourier space in all illumina-
230 tion and viewing directions of the quadrature directions N_θ for $2N_\theta - 1$ azimuthal directions. The contribution $I_m^\uparrow(\mathbf{x},\mathbf{b};\mathbf{m})$ in the direction (Ω_0,Ω_v) is interpolated from the surrounding quadrature directions. Finally, the Jacobian $\mathbf{k}_{x_i} = \frac{\partial y_m(\mathbf{x_i},\mathbf{b};\mathbf{m})}{\partial x_i}$ of $y_m(\mathbf{x},\mathbf{b};\mathbf{m})$ for parameter x_i are calculated as finite differences.

4.2 Scattering layer L_a properties

The layer L_a contains a set of mono-mode aerosol classes v characterized by their single scattering properties, *i.e.*, the single scattering albedo $\omega_{0,v}(\tilde{\lambda})$ and phase function $\Phi_v(\tilde{\lambda},\Omega_g)$ in the spectral bands $\tilde{\lambda}$ at the phase angle Ω_g. These classes define the vertices encompassing the solution space, as illustrated in Fig. (3). The different vertices representing fine and coarse mode aerosols are combined into this layer according to their respective optical thickness $\tau_v(\tilde{\lambda})$ with the total aerosol optical thickness $\tau_a(\tilde{\lambda})$ of the layer being equal to

$$\tau_a(\tilde{\lambda}) = \sum_v \tau_v(\tilde{\lambda}) \tag{3}$$

The phase function $\Phi_v(\tilde{\lambda},\Omega_g)$ of an aerosol vertex is characterized by a limited number N_κ of Legendre coefficients equal to $2N_\theta - 1$ where N_θ is the number of quadrature points used to solve the multiple scattering integral. The choice of this number results from a trade-off between accuracy and computer time. When N_κ is too small, the last Legendre moment is often not equal to zero and the delta-M approximation is applied (Wiscombe, 1977). In that case, the α_d coefficient of the

delta-M approximation is equal to $\Phi_v(N_\kappa)$. The Legendre coefficients κ_j, ~~after application of the delta-M approximation,~~ become

$$c_j = \frac{\kappa_j - \alpha_d}{1 - \alpha_d} \tag{4}$$

and the truncated phase function ~~denoted~~ Φ'_v. The corrected optical thickness $\tau'_v(\tilde{\lambda})$ and single scattering albedo $\omega'_{0,v}(\tilde{\lambda})$ of the corresponding aerosol class become

$$\tau'_v(\tilde{\lambda}) = (1 - \omega_{0,v}\alpha_d)\tau_v(\tilde{\lambda}) \tag{5}$$

and

$$\omega'_{0,v}(\tilde{\lambda}) = \frac{1 - \alpha_d}{1 - \omega_{0,v}\alpha_d}\omega_{0,v}(\tilde{\lambda}) \,. \tag{6}$$

The layer total optical thickness, τ_{L_a}, is the sum of the gaseous, τ_g, the aerosol, τ'_a and the Rayleigh, τ_r, optical depth

$$\tau_{L_a}(\tilde{\lambda}) = \tau_g(\tilde{\lambda}) + \tau'_a(\tilde{\lambda}) + \tau_r(\tilde{\lambda}) \tag{7}$$

with $\tau'_a(\tilde{\lambda}) = \sum_v \tau'_v(\tilde{\lambda})$. The single scattering albedo of the scattering layer is equal to

$$\omega'_0(\tilde{\lambda}) = \frac{\sum_c \omega'_{0,v}(\tilde{\lambda})\,\tau'_v(\tilde{\lambda})}{\tau'_a(\tilde{\lambda})} \tag{8}$$

and the layer average phase function

$$\Phi'(\tilde{\lambda}, \Omega_g) = \frac{\sum_c \Phi'_v(\tilde{\lambda}, \Omega_g)\,\tau'_v(\tilde{\lambda})}{\tau'_a(\tilde{\lambda})} \,. \tag{9}$$

4.3 Gaseous layer properties

It is assumed that only molecular absorption ~~is taking~~ place in layer L_g. The height ~~of level~~ Z_a is used to partition the total column water vapour and ozone concentration in each layer assuming a US76 standard atmosphere vertical profile. This height is not retrieved and is therefore a model parameter of FASTRE which should be derived from some climatological values. T_{L_g} denotes the total transmission of that layer.

Table 1. Relative bias and root mean square error in percentage between FASTRE and the reference RTM in various spectral bands. Wavelengths are given in μm.

Spectral bands (μm)	0.44	0.55	0.67	0.87
Relative bias (%)	-1.1	-0.3	0.0	+0.3
Relative RMSE (%)	2.8	1.8	1.3	1.2

4.4 FASTRE model accuracy

The simple atmospheric vertical structure composed of two layers is the most important assumption of the FASTRE model. In order to evaluate the accuracy of FASTRE, a similar procedure as in Govaerts et al. (2010) has been applied. The outcome of FASTRE has been evaluated against a more elaborated 1D Radiative Transfer Model (RTM) (Govaerts, 2006) where the vertical structure of the atmosphere is explicitly taken into account for sun and viewing angles varying from 0 to 70°, for various types of aerosols, surface reflectance and total column water vapour values. The mean relative bias and relative Root Mean Square Error (RMSE) between the reference model and FASTRE have been estimated in the main spectral bands used for aerosol retrieval. The relative RMSE, R_r, is estimated with

$$R_r = \sqrt{\frac{1}{N} \sum_N \left(\frac{y_m(\mathbf{x}, \mathbf{b}; \mathbf{m}) - y_r(\mathbf{x}, \mathbf{b}; \mathbf{r})}{y_r(\mathbf{x}, \mathbf{b}; \mathbf{r})} \right)^2} \tag{10}$$

where $y_r(\mathbf{x}, \mathbf{b}; \mathbf{m})$ is the TOA BRF calculated with the reference model. In this paper, the FASTRE model solves the RTE using 16 quadrature points N_θ which provides a good compromise between speed and accuracy. Results are shown on Table (1). As can be seen, the relative RMSE between FASTRE and the reference model is typically in the range of $1\% - 3\%$. A similar comparison has been performed against actual PROBA-V observations (Luffarelli et al., 2017). These comparisons show a root mean square error between simulated and actual observations in the range 0.024–0.038.

5 Inversion process

5.1 Overview

Surface reflectance characterisation requires multi-angular observations $\mathbf{y}_{\Omega\widetilde{\Lambda}}$, the acquisition of which can take between several minutes, as is the case for the Multi-angle Imaging SpectroRadiometer (MISR) instrument, and several days, as is the case for the Ocean and Land Colour Instrument (OLCI) on-board Sentinel-3 or the Moderate Resolution Imaging Spectroradiometer (MODIS). In the former case, data are often assumed being acquired almost instantaneously, *i.e.*, with the atmospheric properties remaining unchanged during the acquisition time. Such situation considerably reduces the calculation time required to solve the RTE, as the multiple scattering term $I_m^\uparrow(\mathbf{x}, \mathbf{b}; \mathbf{m})$ needs to be estimated only once per spectral band. In the latter case, atmospheric properties cannot be assumed to be invariant and the multiple scattering contribution needs to be solved for each observation. When geostationary observations are processed, the accumulation period is often reduced to one day, and the assumption that the atmosphere does not change can be converted into an equivalent radiometric uncertainty (Govaerts et al., 2010). Strictly speaking, it should be assumed that atmospheric properties have changed when the accumulation time exceeds several minutes (Luf-

farelli et al., 2016), ~~which increases the number of retrieved state variables to taken into account and~~ ~~therefore the processing time.~~

265   The retrieved state variables in each spectral band $\widetilde{\lambda}$ are composed of the $\mathbf{x_s}$ parameters characterising the state of the surface and the set of aerosol optical thicknesses τ_v for the aerosol vertices that are mixed in layer L_a. Prior information consists of the expected values $\mathbf{x_b}$ of the state variables $\mathbf{x}$ characterising the surface and the atmosphere on one side, and regularization of the spectral and/or temporal variability of τ_v on the other side. Uncertainty matrices $\mathbf{S}_x$ are assigned to this prior infor-

270 mation. Finally, uncertainties in the measurements $\mathbf{S}_y$ are assumed to be normally distributed with zero mean. The inversion process of the FASTRE model will be herein referred to as Combined Inversion of Surface and AeRosol (CISAR) algorithm.

5.2   Cost function

The fundamental principle of Optimal Estimation (OE) is to maximise the probability $P = $

275 $P(\mathbf{x}|\mathbf{y}_{\Omega\widetilde{\Lambda}},\mathbf{x_b},\mathbf{b})$ with respect to the values of the state vector $\mathbf{x}$, conditional to the value of the measurements and any prior information. The conditional probability takes on the quadratic form (Rodgers, 2000; Dubovik et al., 2011):

$$
\begin{aligned}
P(\mathbf{x}) \propto \; &\exp\left[-\big(y_m(\mathbf{x},\mathbf{b};\mathbf{m})-\mathbf{y}_{\Omega\tilde{\Lambda}}\big)^T \mathbf{S}_y^{-1}\big(y_m(\mathbf{x},\mathbf{b};\mathbf{m})-\mathbf{y}_{\Omega\tilde{\Lambda}}\big)\right] \\
&\exp\left[-\big(\mathbf{x}-\mathbf{x}_b\big)^T \mathbf{S}_x^{-1}\big(\mathbf{x}-\mathbf{x}_b\big)\right] \\
&\exp\left[-\mathbf{x}^T \mathbf{H}_a^T \mathbf{S}_a^{-1} \mathbf{H}_a\,\mathbf{x}\right] \\
&\exp\left[-\mathbf{x}^T \mathbf{H}_l^T \mathbf{S}_l^{-1} \mathbf{H}_l\,\mathbf{x}\right]
\end{aligned}
\tag{11}
$$

where the first two terms represent weighted deviations from measurements and the prior state parameters, respectively, the third the AOT temporal smoothness constraints and the fourth the AOT spectral constraint, with respective uncertainty matrices $\mathbf{S}_a$ and $\mathbf{S}_l$. The two matrices $\mathbf{H}_a$ and $\mathbf{H}_l$, representing respectively the temporal and spectral constraints, can be written as block diagonal matrices

$$
\mathbf{H} =
\begin{pmatrix}
\mathbf{H}^{\rho_0} & \mathbf{0} & \mathbf{0} & \mathbf{0} & \mathbf{0} \\
\mathbf{0} & \mathbf{H}^k & \mathbf{0} & \mathbf{0} & \mathbf{0} \\
\mathbf{0} & \mathbf{0} & \mathbf{H}^\theta & \mathbf{0} & \mathbf{0} \\
\mathbf{0} & \mathbf{0} & \mathbf{0} & \mathbf{H}^{\rho_c} & \mathbf{0} \\
\mathbf{0} & \mathbf{0} & \mathbf{0} & \mathbf{0} & \mathbf{H}^\tau
\end{pmatrix}
\tag{12}
$$

where the four blocks $\mathbf{H}^{\rho_0}$, $\mathbf{H}^k$, $\mathbf{H}^\theta$ and $\mathbf{H}^{\rho_c}$ express the spectral constraints between the surface parameters. Their values are set to zero when these constraints are not active. The submatrix $\mathbf{H}_a^\tau$ can also be written using blocks $\mathbf{H}^\tau_{a;\tilde{\lambda},v}$ along the diagonal. For a given spectral band $\tilde{\lambda}$ and aerosol

vertex v, the block $\mathbf{H}^{\tau}_{a;\tilde{\lambda},v}$ is defined as follows

$$
\mathbf{H}^{\tau}_{a;\tilde{\lambda},v}\,\boldsymbol{\tau}_{\tilde{\lambda},v} =
\begin{pmatrix}
1 & -1 & 0 & \dots & \dots \\
0 & 1 & -1 & 0 & \dots \\
\dots & \dots & \dots & \dots & \dots \\
\dots & \dots & \dots & 1 & -1 \\
\dots & \dots & \dots & \dots & 0
\end{pmatrix}
\begin{pmatrix}
\tau_{\tilde{\lambda},v,1} \\
\tau_{\tilde{\lambda},v,2} \\
\vdots \\
\tau_{\tilde{\lambda},v,N_t-1} \\
\tau_{\tilde{\lambda},v,1,N_t}
\end{pmatrix}
\tag{13}
$$

In the same way, the submatrix $\mathbf{H}^{\tau}_l$ can be written using blocks $\mathbf{H}^{\tau}_{l;v,t}$. For a given aerosol vertex v and time t, the block $\mathbf{H}^{\tau}_{l;v,t}$ is defined as follows

$$
\mathbf{H}^{\tau}_{l;v,t}\,\boldsymbol{\tau}_{v,t} =
\begin{pmatrix}
0 & 0 & 0 & \dots & 0 \\
-\frac{\epsilon_2}{\epsilon_1} & 1 & 0 & \dots & 0 \\
0 & -\frac{\epsilon_3}{\epsilon_2} & 1 & \dots & 0 \\
\dots & \dots & \dots & \ddots & 0 \\
\dots & \dots & \dots & -\frac{\epsilon_{N_\lambda}}{\epsilon_{N_\lambda-1}} & 1
\end{pmatrix}
\begin{pmatrix}
\tau_{1,v,t} \\
\tau_{2,v,t} \\
\tau_{3,v,t} \\
\vdots \\
\tau_{N_{\tilde{\lambda}},v,t}
\end{pmatrix}
\tag{14}
$$

where the ϵ_l represents the uncertainties associated with the AOT spectral constraints of the individual vertex v bounding the solution space. The spectral variations of τ_v between band $\tilde{\lambda}_l$ and $\tilde{\lambda}_{l+1}$ writes

$$
\frac{\tau_{\tilde{\lambda}_l,v}}{\tau_{\tilde{\lambda}_{l+1},v}} = \frac{e_{\tilde{\lambda}_l}}{e_{\tilde{\lambda}_{l+1}}}
\tag{15}
$$

where $e_{\tilde{\lambda}_l}$ the extinction coefficient in band $\tilde{\lambda}_l$.

Maximising the probability function in Equation (11) is equivalent to minimising the negative logarithm

$$
J(\mathbf{x}) = J_y(\mathbf{x}) + J_x(\mathbf{x}) + J_a(\mathbf{x}) + J_l(\mathbf{x})
\tag{16}
$$

with

$$
J_y(\mathbf{x}) = \left(y_m(\mathbf{x},\mathbf{b},\Omega) - \mathbf{y}_{\Omega\tilde{\lambda}}\right)\mathbf{S}_y^{-1}\left(y_m(\mathbf{x},\mathbf{b},\Omega) - \mathbf{y}_{\Omega\tilde{\lambda}}\right)^T
\tag{17}
$$

$$
J_x(\mathbf{x}) = \left(\mathbf{x} - \mathbf{x}_b\right)\mathbf{S}_x^{-1}\left(\mathbf{x} - \mathbf{x}_b\right)^T
\tag{18}
$$

$$
J_a(\mathbf{x}) = \mathbf{x}^T\,\mathbf{H}_a^T\,\mathbf{S}_a^{-1}\,\mathbf{H}_a\,\mathbf{x}
\tag{19}
$$

$$
J_l(\mathbf{x}) = \mathbf{x}^T\,\mathbf{H}_l^T\,\mathbf{S}_l^{-1}\,\mathbf{H}_l\,\mathbf{x}
\tag{20}
$$

Notice that the cost function J is minimized with respect to the state variable $\mathbf{x}$, so that the derivative of J is independent of the model parameters $\mathbf{b}$ which therefore cannot be part of the solution. The need for angular sampling to document the surface anisotropy leads to an unbalanced size of n_x and n_y with $n_y > n_x$ where n_y and n_x represents the number of observations and state variables respectively. According to Dubovik et al. (2006), these additional observations should improve the retrieval as, from a statistical point of view, repeating the same observation implies that the variance of repeated similar observations should decrease. Accordingly, the magnitude of the

elements of the covariance matrix should decrease as $1/\sqrt{n_y}$. Thus, repeating similar observations results in some enhancements of retrieval accuracy which should be proportional to the ratio n_y/n_x. Hence, the cost function which is actually minimized is $J_s(\mathbf{x}) = J_y(\mathbf{x}) + n_y/n_x \left(J_x(\mathbf{x}) + J_a(\mathbf{x}) + J_l(\mathbf{x})\right)$.

5.3 Retrieval uncertainty estimation

The retrieval uncertainty is based on the OE theory, assuming a linear behaviour of $y_m(\mathbf{x}, \mathbf{b}; \mathbf{m})$ in the vicinity of the solution $\hat{\mathbf{x}}$. Under this condition, the retrieval uncertainty $\sigma_{\hat{\mathbf{x}}}$ is determined by the shape of $J(\mathbf{x})$ at $\hat{\mathbf{x}}$

$$\sigma_{\hat{\mathbf{x}}}^2 = \left(\frac{\partial^2 J_s(\mathbf{x})}{\partial \mathbf{x}^2}\right)^{-1} = \left(\mathbf{K}_x^T \mathbf{S}_y^{-1} \mathbf{K}_x + \mathbf{S}_x^{-1} + \mathbf{H}_a^T \mathbf{S}_a^{-1} \mathbf{H}_a + \mathbf{H}_l^T \mathbf{S}_l^{-1} \mathbf{H}_l\right)^{-1} \tag{21}$$

where $\mathbf{K}_x$ is Jacobian matrix of $y_m(\mathbf{x}, \mathbf{b}; \mathbf{m})$ calculated in $\hat{\mathbf{x}}$. Combining Equations (21) and (8), the uncertainty in the retrieval of ω_0 in band $\tilde{\lambda}$ writes

$$\sigma_{\hat{\omega}_0}^2(\tilde{\lambda}) = \sum_v \left(\frac{\omega_{0,v}(\tilde{\lambda}) - \omega_0(\tilde{\lambda})}{\tau_a(\tilde{\lambda})}\right)^2 \sigma_{\hat{\tau}_v}^2(\tilde{\lambda}) \tag{22}$$

A similar equation can be derived for the estimation of σ_g^2.

5.4 Acceleration methods

The minimization of Equation (16) relies on an iterative approach with $y_m(\mathbf{x}, \mathbf{b}; \mathbf{m})$ and the associated Jacobians $\mathbf{K}_x$ being estimated at each iteration. In order to reduce the calculation time dedicated to the estimation of $y_m(\mathbf{x}, \mathbf{b}; \mathbf{m})$ and $\mathbf{K}_x$, a series of methods have been implemented. All quantities that do not explicitly depend on the state variables, such as the observation conditions $\mathbf{m}$, model parameters $\mathbf{b}$, quadrature point weight, *etc*, are computed only once prior to the optimization.

When solving the RTE, the estimation of the multiple scattering term is by far the most time-consuming step. Hence, during the iterative optimisation process, when the change $\Delta\tau_a(\tilde{\lambda})$ of $\tau_a(\tilde{\lambda})$ between iteration j and $j+1$ is small, the multiple scattering contribution at iteration $j+1$ is estimated with

$$I_m^\uparrow(\tau_a(j+1, \tilde{\lambda}), \mathbf{b}; \mathbf{m}) = I_m^\uparrow(\tau_a(j, \tilde{\lambda}), \mathbf{b}; \mathbf{m}) + \frac{\partial I_m^\uparrow(\tau_a(j, \tilde{\lambda}), \mathbf{b}; \mathbf{m})}{\partial \tau_a} \Delta\tau_a(\tilde{\lambda}) \tag{23}$$

This approximation is not used twice consecutively to avoid inaccurate results, and the single scattering contribution is always explicitly estimated.

6 Algorithm performance evaluation

6.1 Experimental setup

A simple experimental setup based on simulated data has been defined to illustrate the behaviour of the CISAR algorithm as a function of the delineated solution space. More specifically, its capability

 List of aerosol properties used for the simulations. The parameters r_{mf} and r_{mc} are the median fine and coarse mode radii expressed in μm. Their respective standard deviations are $\sigma_{r_{mf}}$ and $\sigma_{r_{mc}}$. The parameters n_r and n_i are the real and imaginary part of the refractive index in the indicated bands. N_f and N_c are the fine and coarse mode particle concentration in number of particles per cm^3.

Centre band in μm			0.44	0.55	0.67	0.87		
Type	r_{mf}	r_{mc}	n_i	n_r	n_r	n_r	N_f	N_c
F0	0.08	-	1.3958	1.3932	1.3909	1.3879	-	-
F1	0.10	0.93	1.4189	1.4269	1.4357	1.4417	9.587	0.002
F2	0.08	0.77	1.4985	1.5201	1.5436	1.5417	8.975	0.024
	$\sigma_{r_{mf}}$	$\sigma_{r_{mc}}$	n_i	n_i	n_i	n_i		
F0	0.45	-	0.0123	0.0123	0.0122	0.0121	-	-
F1	0.43	0.62	0.0057	0.0055	0.0053	0.0051		
F2	0.50	0.62	0.0054	0.0047	0.0040	0.0036		

to continuously sample the $[g,\omega_0]$ solution space is examined in detail. For the sake of simplicity, a noise-free multi-angular observation vector $\mathbf{y}_{\Omega\widetilde{\Lambda}}$, where Ω expresses the illumination and viewing

315 geometries, is assumed to be acquired instantaneously in the principal plane and in the spectral bands listed in Table (1). An uncertainty of 3% is assumed in matrix $\mathbf{S}_y$. In this ideal configuration, the Sun Zenith Angle (SZA) is set to 30°. It is also assumed that the surface parameters are known a priori with zero bias and an uncertainty of 0.03 for each RPV parameter, though these parameters are allowed to vary. Such assumption can be justified applying the method and associated results

320 described in Wagner et al. (2010). No prior information is assumed for the aerosol optical thickness, *i.e.*, the prior uncertainty is set to very large values. Only regularization on the spectral variations of τ_a is applied.

Table 3. Micro-physical parameter values for the four FA, FN, CS, CL vertices in the selected spectral bands. Radius are given in μm

Centre band in μm			0.44	0.55	0.67	0.87	0.44	0.55	0.67	0.87
Type	r_m	σ_{r_m}	n_r	n_r	n_r	n_r	n_i	n_i	n_i	n_i
FN	0.08	0.45	1.3958	1.3932	1.3909	1.3879	0.0006	0.0006	0.0006	0.0006
FA	0.08	0.45	1.3958	1.3932	1.3909	1.3879	0.0207	0.0207	0.0207	0.0205
CS	0.30	0.55	1.4889	1.4878	1.4845	1.4763	0.0029	0.0029	0.0029	0.0029
CL	1.00	0.55	1.4889	1.4878	1.4845	1.4763	0.0029	0.0029	0.0029	0.0029

The CISAR algorithm performance evaluation is based on a series of experiments corresponding to different selections of aerosol properties, both for the forward simulation of the observations

325 and their inversion. Three different aerosol models are used in the forward simulations: F0 which only contains small particles, F1 which contains a dual-mode particle size distribution dominated

by small particles, and F2 composed of a dual-mode distribution dominated by the coarse particles. Table (2) contains the values of the size distribution and refractive indices of these aerosol classes. Corresponding values for the four FA, FN, CL, CS vertices enclosing the solution space as illustrated in Fig. (3) are given in Table (3). When the observations simulated with aerosol types F0, F1 or F2 are inverted, the list of vertices actually used depends on the type of experiments indicated in Table (4). ~~The objective of these experiments is to illustrate the impact of the selected solution space on the retrieved aerosol properties.~~ For all these scenarios, an AOT of 0.4 at 0.55μm is assumed.

Table 4. List of experiments the name of which is provided in the first column. The active vertices in each experiment~~s~~ are indicated with the $\times$ symbol. The last column indicates the name of the aerosol model used to simulate the observations.

Exp.	Active vertices				Forward type
	FA	FN	CS	CL	
F00	$\times$	$\times$			F0
F10	$\times$	$\times$			F1
F11	$\times$	$\times$	$\times$		F1
F12	$\times$	$\times$		$\times$	F1
F13	$\times$	$\times$	$\times$	$\times$	F1
F21	$\times$	$\times$	$\times$		F2
F22	$\times$	$\times$		$\times$	F2
F23	$\times$	$\times$	$\times$	$\times$	F2

Table 5. Values of the surface RPV parameters ~~as~~ used ~~in the experiments for the~~ prior information. ~~Wavelengths are given in μm.~~

Wavelength	ρ_0	k	Θ	ρ_c
0.44	0.025	0.666	-0.150	0.125
0.55	0.047	0.657	-0.114	0.023
0.67	0.056	0.710	-0.096	0.025
0.87	0.238	0.706	-0.019	0.030

Values used for the RPV parameters in the four selected bands are indicated in Table (5). They correspond to typical BRF values that would be observed over a vegetated surface with a leaf area index value of 3 and a bright underlying soil.

The primary objective of these experiments is to illustrate the behaviour of the proposed algorithm as a function of the selected vertices. It is therefore not intended to demonstrate that the algorithm can work in all possible conditions. Examples of retrieval against actual satellite observations can be found in Luffarelli et al. (2016).
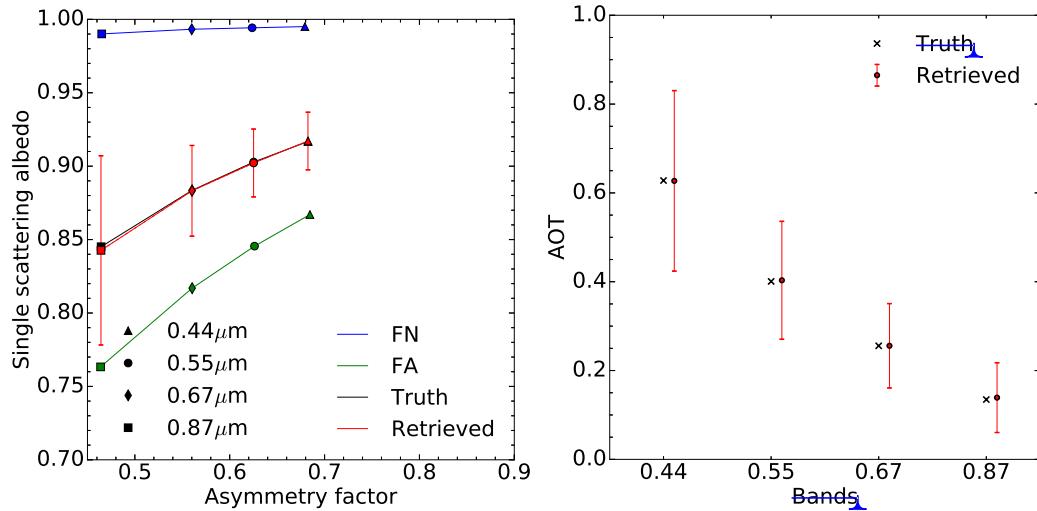
Fig. 5. Left panel: Results of experiment F00 in the $[g, \omega_0]$ space. The aerosol vertices used for the inversion are FN (blue) and FA (green). The forward aerosol properties are shown in black and the retrieved ones in red. Vertical and horizontal red bars indicate the uncertainty, if any, of the retrieved values. **Right panel**: Retrieved AOT in the four processed spectral bands (red circles). The retrieval uncertainty is shown with the vertical red lines. True values are indicated with black crosses.

6.2 Results

6.2.1 Experiment F00

The purpose of the first experiment (F00) is to demonstrate that the CISAR algorithm can accurately retrieve aerosol properties in a simple situation, showing therefore that the inversion process works correctly. The F0 aerosol class used to simulate the observations is only composed of fine particles with a median radius of 0.08μm, *i.e.*, the same value as for the FN and FA vertices used for the inversion. Hence, only the imaginary part of the index of refraction differs from the values used for the generation of these two vertices, the real part being set to 1.4. With such a retrieval configuration restricted to the use of only two vertices, the solution space for each wavelength is limited to a straight line between the two vertices.

Results are shown in Fig. (5) for the atmosphere and Table (6) for the surface. The asymmetry factor g and single scattering albedo ω_0 are almost exactly retrieved. There is practically no uncertainty in the retrieval of g because of the constraints imposed by the fact that the particle radius is the same as for the F0 aerosol class. The estimated single scattering albedo uncertainty is much larger than the asymmetry one, though the retrieved values match exactly the true ones. The retrieved AOT is also in very good agreement with the true values as can be seen on the right panel in Fig. (5). To further evaluate the performance of the CISAR algorithm, the retrieval error ϵ_τ is defined as the difference between the retrieved and the true AOT values. Results are summarised in Table (7). This

first experiment demonstrates that it is possible to retrieve the properties of the aerosol class F0 as a

360 linear combination of the vertices FA and FN when only the absorption varies, the particle median

radius being constant.

A comparison between Tables (5) and (6) shows that the surface parameters are very accurately retrieved. As stated in Section (6.1), prior information on the magnitude of the RPV parameter is assumed unbiased with an uncertainty of 0.03. The corresponding posterior uncertainties exhibit a

365 significant decrease for the ρ_0 parameter at all wavelengths. A similar behaviour is not observed

for the other parameters. As explained in Wagner et al. (2010), the k and Θ parameters, controlling

the surface reflectance anisotropy, are strongly correlated with amount atmospheric scattering. Con-

sequently, the retrieved uncertainties decrease with ~~the~~ wavelengths, *i.e.*, as a function of the actual

AOT. Despite the observations are taking place in the principal plane, the posterior uncertainty on the

370 hot spot parameter remains equal to the prior one as a result of atmospheric scattering. This fact is

attributed to the relatively high value of the true AOT, and the consequent amount of scattering ~~able~~

~~to attenuate~~ the hot spot ~~effects~~. Results for the surface parameter retrieval exhibits a very similar

behaviour for the other experiments and will not be shown.

Table 6. Values of the retrieved surface RPV parameters and associated uncertainties for experiment F00. Wavelengths are given in μm.

	Value				Uncertainty			
Band	ρ_0	k	Θ	ρ_c	ρ_0	k	Θ	ρ_c
				Posterior				
0.44	0.025	0.666	-0.150	0.125	0.006	0.030	0.030	0.030
0.55	0.047	0.657	-0.116	0.023	0.004	0.029	0.028	0.030
0.67	0.056	0.711	-0.096	0.025	0.004	0.028	0.026	0.030
0.87	0.238	0.705	-0.020	0.029	0.011	0.025	0.017	0.030

6.2.2 Experiment F10

375 Let us now examine the case where both ~~the~~ r_m and n_i ~~used to describe the forward aerosol proper-~~

~~ties~~ differ from those of the vertices used for the inversion. ~~For that purpose, aerosol~~ type F1 is used

for the forward simulation with $r_{mf} = 0.1\mu$m for the predominant fine mode and $r_{mc} = 0.93\mu$m for

the coarse mode. The same aerosol vertices as in experiments F00 are used for the inversion.

The results in Fig. (6) show that ω_0 is reasonably well retrieved unlike the g parameter, which

380 is systematically underestimated. At any given wavelengths, it is not possible to retrieve g values

outside the bounds defined by the FA and FN vertices. Consequently, the retrieved AOT values are

underestimated by about 10% (Table 7). Additionally, the estimated error on g is largely underesti-

mated. This example illustrates the retrieval failure when the actual solution lays outside the $[g, \omega_0]$

space defined by the active vertices.
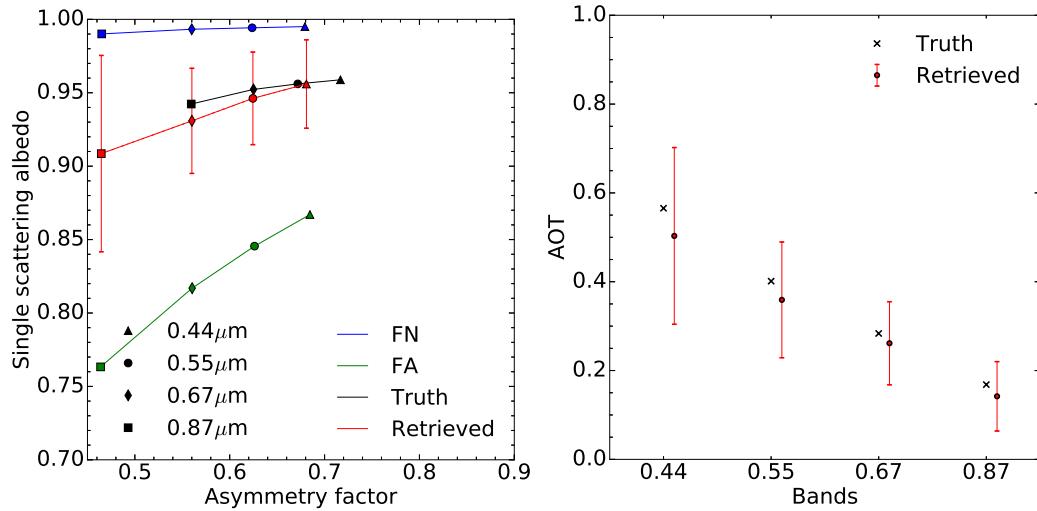
Fig. 6. Same as Fig. (5) but for experiment F10.

Table 7. Retrieved AOT error and uncertainties for the six experiments ~~in the four processed bands~~. The ϵ_τ ~~symbol is the~~ error calculated as the difference between the retrieved ~~value and the truth~~, δ_τ the relative error in percent and σ_τ the retrieval uncertainty estimated with Equation (21).

BAND	0.44			0.55			0.67			0.87		
EXP	ϵ_τ	δ_τ (%)	σ_τ	ϵ_τ	δ_τ (%)	σ_τ	ϵ_τ	δ_τ (%)	σ_τ	ϵ_τ	δ_τ (%)	σ_τ
F00	0.001	-0.1	0.203	-0.002	0.6	0.133	-0.000	0.0	0.095	-0.004	3.3	0.079
F10	0.062	-11.0	0.199	0.042	-10.5	0.130	0.022	-7.8	0.094	0.026	-15.6	0.078
F11	0.005	-0.9	0.239	-0.021	5.3	0.164	-0.037	13.2	0.125	-0.047	27.8	0.095
F12	0.041	-7.3	0.228	0.013	-3.3	0.152	-0.004	1.5	0.113	-0.015	8.6	0.089
F13	-0.001	0.1	0.295	-0.028	6.9	0.199	-0.041	14.5	0.145	-0.051	30.5	0.103
F21	0.018	-3.9	0.252	0.037	-9.2	0.172	0.042	-11.9	0.129	0.071	-22.9	0.096
F22	-0.018	3.9	0.236	-0.007	1.8	0.158	-0.004	1.1	0.116	0.008	-2.6	0.090
F23	-0.041	8.8	0.296	-0.031	7.8	0.200	-0.027	7.5	0.145	-0.018	6.0	0.103

385 6.2.3 Experiments F11 - F13

In order to improve the retrieval of the F1 aerosol class properties, the additional aerosol CS vertex ~~has been~~ added in layer L_a during the inversion process~~, i.e., a coarse mode with $r_m = 0.3\mu m$.~~ Results of experiment F11 are displayed ~~on~~ Fig. (7). Retrieved g values are no longer ~~systematically~~ underestimated. The single scattering albedo is slightly underestimated. It should be noted that
390 the estimated uncertainty associated with g increases with wavelength and is particularly large at $0.87\mu m$, but rather underestimated at $0.44\mu m$. The improvement in the AOT retrieval accuracy is noticeable in the $0.44\mu m$ and $0.55\mu m$ bands where the magnitude of ϵ_r is reduced from 0.062 to

0.005 and from 0.042 to -0.021 respectively (Table 7). At larger wavelengths, the benefit of adding the CS vertex is less noticeable though the magnitude of ϵ_r remains below 0.05. Finally, the retrieval

395   uncertainty slightly increases from 0.199 up to 0.239 in the 0.44μm band because of the use of additional state variables τ_v associated with the inclusion of an additional vertex.
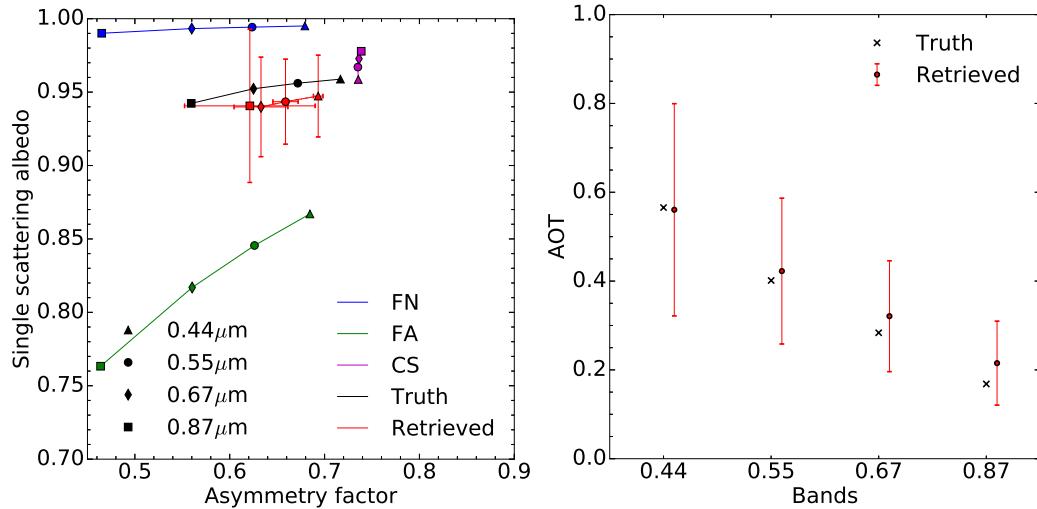
Fig. 7. Same as Fig. (5) but for experiment F11.
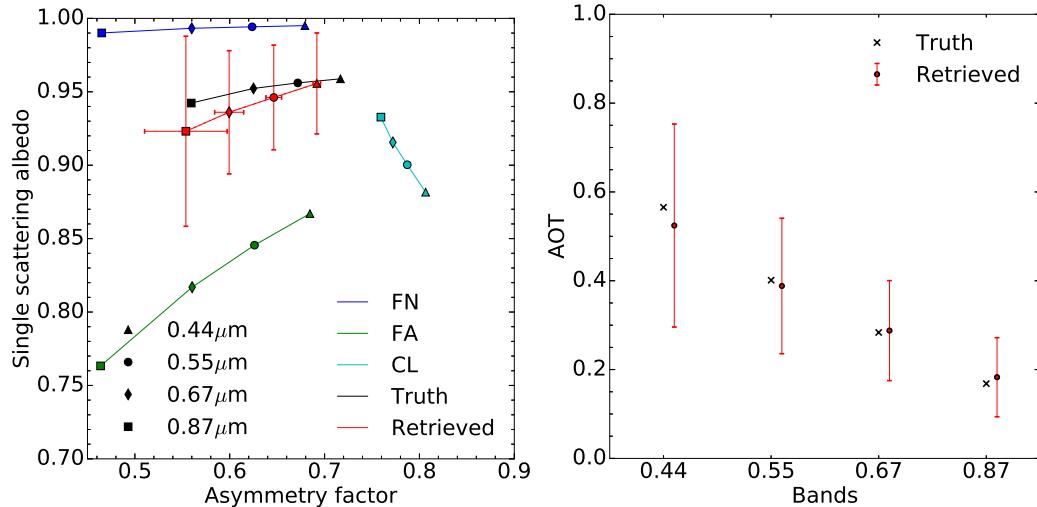
Fig. 8. Same as Fig. (5) but for experiment F12.

For experiment F12, the CS vertex is substituted by vertex CL which has a median radius of 1.0μm. The use of this vertex instead of CS considerably improves the retrieval of g and of ω_0 at large wavelengths (Fig. 8). As can be seen in Fig. (2), the sensitivity of aerosol single scattering properties

400   to particle median radius and imaginary part of the refractive index depends on the wavelength.
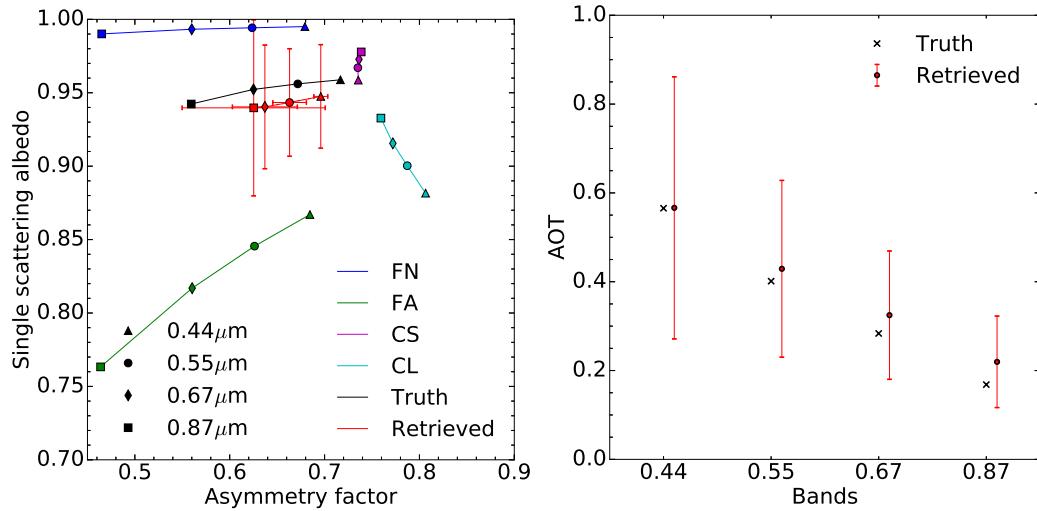
Fig. 9. Same as Fig. (5) but for experiment F13.

Hence, a similar behaviour of the algorithm in all wavelengths should not be expected. The errors ϵ_τ in this experiment ~~F12~~ are further reduced compared to experiment F11 with the exception of the 0.44μm band. The CISAR algorithm manages to correctly retrieve the total AOT.

Finally, the inversion ~~has been~~ performed using all four vertices (Fig. 9) ~~in experiment F13~~.
405 This additional degree of freedom translates into an increase of the estimated uncertainty $\sigma_{\hat\tau}$ as a result of the large number of possible way to combine these four vertices to retrieve the properties of the aerosol class F1. In other words, adding two coarse mode vertices does not improve the characterization of F1. The actual benefit of adding this fourth vertex is therefore not straightforward, and should be noted that increasing the number of vertices impacts the computational time. This
410 series of ~~simple three~~ experiments has shown that the use of the FN, FA and CL vertices provides the best combination for the retrieval of the properties of aerosol class F1. With this combination, the FN and FA vertices allow to control the amount of radiation absorbed by the aerosols and the CL vertex the effects of the particle size.

6.2.4 Experiments F21 - F23

415 The retrieval of aerosol class F2, a dual-mode particle size distribution dominated by coarse particles, is now examined. This class is composed of a fine mode radius r_{mf} of 0.08μm and coarse mode ~~one~~ r_{mc} of 0.77μm. As for the retrieval of the F1 aerosol class, three combinations of vertices have been explored, *i.e.*, (FN, FA, CS) for experiment F21 (Fig. 10), (FN, FA, CL) for experiment F23 (Fig. 11) and ~~finally~~ (FN, FA, CS, CL) for experiment F22 (Fig. 11). Essentially the same conclusions
420 hold as for the retrieval of aerosol class F1. The retrieval of F2-class properties expressed as a linear combination of the (FN, FA, CL) vertices provides the best solution. ~~Values of~~ both g and ω_0 ~~are~~ well retrieved at all wavelengths.
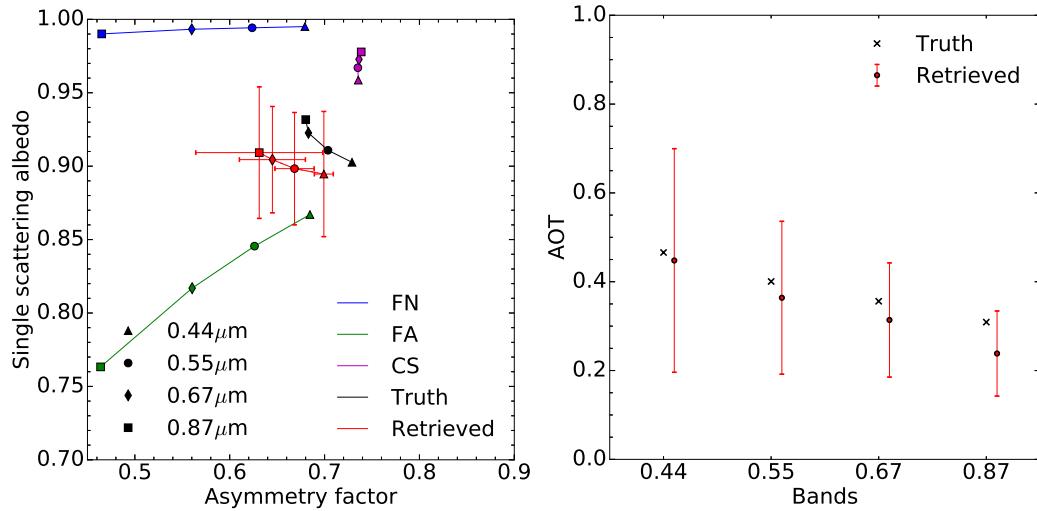
Fig. 10. Same as Fig. (5) but for experiment F21.
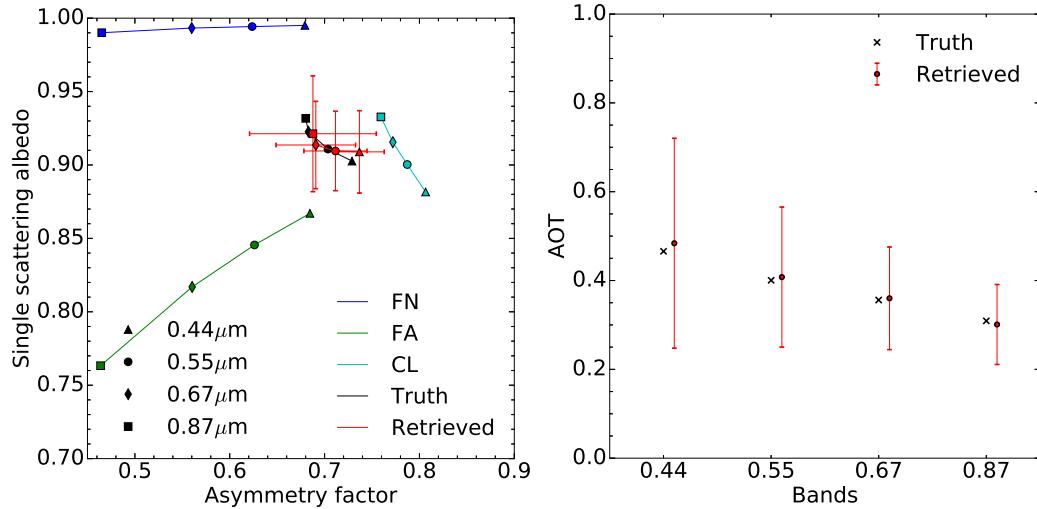
Fig. 11. Same as Fig. (5) but for experiment F22.

7 Discussion and conclusion

This paper describes the CISAR algorithm designed for the joint retrieval of surface reflectance and
425 aerosol properties. Previous attempts to perform such joint retrieval have been reviewed, discussing
their advantages and weaknesses. ~~That analysis revealed that retrieval~~ methods based on OE applied
only to a limited number of aerosol classes represent a major drawback as it does not permit a con-
tinuous variation of the state variables in the solution space. The new method presented in this paper
specifically addresses this issue, allowing continuous variations of the aerosol single scattering prop-
430 erties in the solution space without ~~having~~ the aerosol micro-physical properties explicitly appearing
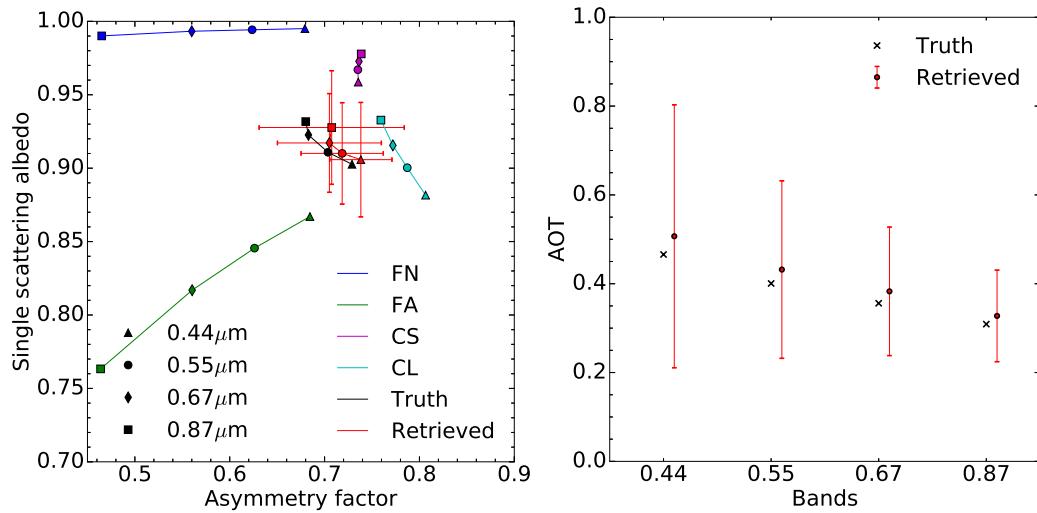
Fig. 12. Same as Fig. (5) but for experiment F23.

as state variables.

A fast forward radiative transfer model has been designed ~~for this purpose~~, which solves the radiative transfer equation without relying on pre-computed look-up tables. This model considers ~~only~~ two layers ~~in the atmosphere~~. The upper layer only hosts molecular absorption. The lower layer accounts for both absorption and scattering processes due to aerosols and molecules and is radiative coupled with the surface represented with the RPV BRF model. Single scattering aerosol properties in this layer are expressed as a linear combination of the properties of vertices enclosing the solution space.

A series of different experiments has been devised to analyse the behaviour of the CISAR algorithm and its capability to retrieve aerosol single scattering properties as well as optical thickness. This discussion focuses on the retrieval of aerosol classes ~~F1~~ dominated by the fine mode ~~and F2 dominated~~ by ~~the~~ coarse mode. These two classes have pretty different spectral behaviour in the $[g, \omega_0]$ space and yet the CISAR algorithm is capable of retrieving the corresponding single scattering properties in both cases.

These experiments illustrate the possibility to use Equations (8) and (9) for the continuous retrieval of the aerosol single scattering albedo and ~~phase function properties in the solution space.~~ These equations assume a linear behaviour of ω_0 and g in the solution space ~~illustrated in Fig. (3) as a function of the variations of the aerosol micro physical properties~~. Such assumptions have proven to be valid for the case addressed in experiment F00. This assumption is not exactly true for the retrieval of more realistic aerosol classes composed of a fine and a coarse particle size modes. However, the retrieved aerosol single scattering properties are derived much more accurately than with a method based on a limited number of predefined aerosol classes as in Govaerts et al. (2010) where ~~only~~ the single scattering properties of ~~the~~ predefined classes ~~can be exactly~~ retrieved. It thus

represents a major improvement with respect to these type of retrieval approaches without requiring the use of a large number of state variables as in the method proposed by Dubovik et al. (2011), ~~where aerosol micro-physical properties are explicitly included in the set of retrieved state variables~~.

The choice of the vertices outlining the $[g, \omega_0]$ solution space is critical. In these experiments, best retrieval is obtained using three vertices, *i.e.*, one vertex composed of small weakly absorbing particles (FN), one vertex composed of small absorbing particles (FA) and one vertex composed of large particles (CL). The use of a fourth vertex (CS) does not improve the retrieval and increases the estimated retrieval uncertainty.

This set of experiments represents ideal conditions, *i.e.*, noise-free observations in the principal plane with no bias on the surface prior. This choice is motivated by the need to keep the result interpretation simple, ~~the primary objective being~~ to illustrate how the new retrieval concept developed in this paper works. These experiments show the possibility to retrieve aerosol single scattering properties within the solution space provided it is correctly bounded by the vertices. It is clear that adding noise in the observations will degrade the quality of the retrieval. Similar conclusions can hold in case the observations are taking place far from the principal plane where most of the angular variations occur. It should be stressed that this approach can also be applied for the retrieval of similar properties within a single cloud layer or a mixture of cloud and aerosol.

~~Such an algorithm therefore represents a decisive improvement with respect to the method proposed by Govaerts et al. (2010) which retrieves the aerosol optical thickness only for the very limited number of pre-defined aerosol classes. The CISAR algorithm allows a continuous variation of the aerosol single scattering properties adding only a limited number of state variables, *i.e.*, the optical thickness of each vertices.~~

8 Acknowledgements

Acknowledgements. The authors would like to thanks the reviewers for their fruitful suggestions.

References

Cox, C. and Munk, W.: Measurement of the Roughness of the Sea Surface from Photographs of the Sun's Glitter, Journal of the Optical Society of America, 44, 838–850, doi:10.1364/JOSA.44.000838, 1954.

Diner, D. J., Hodos, R. A., Davis, A. B., Garay, M. J., Martonchik, J. V., Sanghavi, S. V., von Allmen, P., Kokhanovsky, A. A., and Zhai, P.: An optimization approach for aerosol retrievals using simulated MISR radiances, Atmospheric Research, 116, 1–14, doi:10.1016/j.atmosres.2011.05.020, 2012.

Dubovik, O., Sinyuk, A., Lapyonok, T., Holben, B. N., Mishchenko, M., Yang, P., Eck, T. F., Volten, H., Munoz, O., Veihelmann, B., van der Zande, W. J., Leon, J. F., Sorokin, M., and Slutsker, I.: Application of spheroid models to account for aerosol particle nonsphericity in remote sensing of desert dust, Journal of Geophysical Research-Atmospheres, 111, 11 208–11 208, 2006.

Dubovik, O., Herman, M., Holdak, A., Lapyonok, T., Tanr, D., Deuz, J. L., Ducos, F., Sinyuk, A., and Lopatin, A.: Statistically optimized inversion algorithm for enhanced retrieval of aerosol properties from spectral multi-angle polarimetric satellite observations, Atmospheric Measurement Techniques, 4, 975–1018, 2011.

Fischer, J. and Grassl, H.: Radiative transfer in an atmosphere-ocean system: an azimuthally dependent matrix-operator approach, Applied Optics, 23, 1032–1039, 1984.

Govaerts, Y. and Lattanzio, A.: Retrieval Error Estimation of Surface Albedo Derived from Geostationary Large Band Satellite Observations: Application to Meteosat-2 and -7 Data, Journal of Geophysical Research, 112, doi:10.1029/2006JD007 313, 2007.

Govaerts, Y., Luffarelli, M., and Damman, A.: Effects of Sky Radiation on Surface Reflectance: Implications on The Derivation of LER from BRF for the Processing of Sentinel-4 Observations, in: Living Planet Symposium 2016, Prague, Czech Republic, Prague, Czech Republic, 2016.

Govaerts, Y. M.: RTMOM V0B.10 User's Manual, 2006.

Govaerts, Y. M., Lattanzio, A., Taberner, M., and Pinty, B.: Generating global surface albedo products from multiple geostationary satellites, Remote Sensing of Environment, 112, 2804–2816, doi:10.1016/j.rse.2008.01.012, http://www.sciencedirect.com/science/article/pii/S0034425708000412, 2008.

Govaerts, Y. M., Wagner, S., Lattanzio, A., and Watts, P.: Joint retrieval of surface reflectance and aerosol optical depth from MSG/SEVIRI observations with an optimal estimation approach: 1. Theory, Journal of Geophysical Research, 115, doi:10.1029/2009JD011 779, 2010.

Hess, M., Koepke, P., and Schult, I.: Optical properties of aerosols and clouds: The software package OPAC, Bulletin of the American Meteorological Society, 79, 831–844, 1998.

Kokhanovsky, A. A., Deuz, J. L., Diner, D. J., Dubovik, O., Ducos, F., Emde, C., Garay, M. J., Grainger, R. G., Heckel, A., Herman, M., Katsev, I. L., Keller, J., Levy, R., North, P. R. J., Prikhach, A. S., Rozanov, V. V., Sayer, A. M., Ota, Y., Tanr, D., Thomas, G. E., and Zege, E. P.: The inter-comparison of major satellite aerosol retrieval algorithms using simulated intensity and polarization characteristics of reflected light, Atmos. Meas. Tech., 3, 909–932, doi:10.5194/amt-3-909-2010, 2010.

Lattanzio, A., Schulz, J., Matthews, J., Okuyama, A., Theodore, B., Bates, J. J., Knapp, K. R., Kosaka, Y., and Schller, L.: Land Surface Albedo from Geostationary Satelites: A Multiagency Collaboration within SCOPE-CM, Bulletin of the American Meteorological Society, 94, 205–214, doi:10.1175/BAMS-D-11-00230.1, 2013.

Liu, Q. and Ruprecht, E.: Radiative transfer model: matrix operator method, Applied Optics, 35, 4229–4237,

1996.

Luffarelli, M., Govaerts, Y., and Damman, A.: Assessing hourly aerosol properties retrieval from MSG/SEVIRI
520   observations in the framework of aeroosl-cci2, in: Living Planet Symposium 2016, Prague, Czech Republic,
    Prague, Czech Republic, 2016.

Luffarelli, M., Govaerts, Y., Goossens, C., Wolters, E., and Swinnen, E.: Joint retrieval of surface reflectance
    and aerosol properties from PROBA-V observations, part I: algorithm performance evaluation, in: Proceed-
    ings of MultiTemp 2017, Bruges, Belgium, 2017.

525 Manolis, I., Grabarnik, S., Caron, J., Bzy, J.-L., Loiselet, M., Betto, M., Barr, H., Mason, G., and Meynart, R.:
    The MetOp second generation 3MI instrument, p. 88890J, doi:10.1117/12.2028662, 2013.

Marquardt, D.: An Algorithm for Least-Squares Estimation of Nonlinear Parameters, SIAM Journal on Applied
    Mathematics, 11, 431–441, 1963.

Pinty, B., Roveda, F., Verstraete, M. M., Gobron, N., Govaerts, Y., Martonchik, J. V., Diner, D. J., and Kahn,
530   R. A.: Surface albedo retrieval from Meteosat: Part 1: Theory, Journal of Geophysical Research, 105,
    18 099–18 112, 2000a.

Pinty, B., Roveda, F., Verstraete, M. M., Gobron, N., Govaerts, Y., Martonchik, J. V., Diner, D. J., and Kahn,
    R. A.: Surface albedo retrieval from Meteosat: Part 2: Applications, Journal of Geophysical Research, 105,
    18 113–18 134, 2000b.

535 Rahman, H., Pinty, B., and Verstraete, M. M.: Coupled surface-atmosphere reflectance (CSAR) model. 2.
    Semiempirical surface model usable with NOAA Advanced Very High Resolution Radiometer Data, Journal
    of Geophysical Research, 98, 20,791–20,801, 1993.

Rodgers, C. D.: Inverse methods for atmospheric sounding, Series on Atmospheric Oceanic and Planetary
    Physics, World Scientific, 2000.

540 Schuster, G. L., Dubovik, O., Holben, B. N., and Clothiaux, E. E.: Inferring black carbon content and specific
    absorption from Aerosol Robotic Network (AERONET) aerosol retrievals, Journal of Geophysical Research,
    110, S1017–S1017, 2005.

Serene, F. and Corcoral, N.: PARASOL and CALIPSO : Experience Feedback on Operations of Micro and
    Small Satellites, in: SpaceOps 2006 Conference, American Institute of Aeronautics and Astronautics, dOI:
545   10.2514/6.2006-5919, 2006.

Vermote, E. F., Tanré, D., Deuzé, J. L., Herman, M., and Morcrette, J. J.: Second simulation of the satellite
    signal in the solar spectrum, 6S: An overview, IEEE TGARS, 35, 675–686, 1997.

Wagner, S. C., Govaerts, Y. M., and Lattanzio, A.: Joint retrieval of surface reflectance and aerosol optical depth
    from MSG/SEVIRI observations with an optimal estimation approach: 2. Implementation and evaluation,
550   Journal of Geophysical Research, 115, doi:10.1029/2009JD011 780, 2010.

Wiscombe, W. J.: The Delta-M Method: Rapid Yet Accurate Radiative Flux Calculations for Strongly Asym-
    metric Phase Functions, Journal of Atmospheric Sciences, 34, 1408–1422, 1977.